

QUANTUM SIMULATION

Coherent evolution of superexchange interaction in seconds-long optical clock spectroscopy

William R. Milner^{1*}, Stefan Lannig¹, Mikhail Mamaev^{1,2}, Lingfeng Yan¹, Anjun Chu^{1,2}, Ben Lewis¹, Max N. Franke¹, Ross B. Hutson¹, Ana Maria Rey^{1,2}, Jun Ye^{1*}

Scaling up the performance of atomic clocks requires understanding complex many-body Hamiltonians to ensure meaningful gains for metrological applications. Here we use a degenerate Fermi gas loaded into a three-dimensional optical lattice to study the effect of a tunable Fermi-Hubbard Hamiltonian. The clock laser introduces a spin-orbit coupling spiral phase and breaks the isotropy of superexchange interactions, leading to XXZ-type spin anisotropy. By tuning the lattice confinement and applying imaging spectroscopy, we map out favorable atomic coherence regimes. We transition through various interaction regimes and observe coherent superexchange, tunable through on-site interaction and site-to-site energy shift, affecting the Ramsey fringe contrast over timescales >1 second. This study lays the groundwork for using a three-dimensional optical lattice clock to probe quantum magnetism and spin entanglement.

Optical lattice clocks are advancing studies of fundamental physics, metrology, and quantum simulation (1–7). By controlling all external perturbations to the ground and metastable “clock” state, each one of the confined atoms becomes a pristine, two-level system. With clock precision limited fundamentally by quantum projection noise (8), a natural approach for improving clock performance is to probe the largest possible number of atoms combined with the longest possible coherence time. However, in a densely packed sample of atoms, outstanding challenges remain, including maximizing the coherence time for clock precision and evaluating systematic effects for clock accuracy. Often it is desirable to minimize atomic interactions to enhance single-particle coherence and control systematic effects. At the same time, as the understanding of these interactions becomes more sophisticated, we can engineer a large, coherent spin ensemble with interaction precisely controlled to introduce and optimize quantum coherence, correlation, and entanglement to advance the frontier of quantum metrology (9–12).

With the ease of geometry tunability, optical lattices provide a versatile platform to confine large numbers of atoms and control their interactions and motion. Over the past two decades, progress in clock precision (13, 14) has been largely advanced by the study and control of interactions in one-dimensional (1D) optical lattice clocks. The corresponding interaction dynamics are well described by a collective spin model (15, 16) that includes both on-site p -wave interactions and off-site s -wave interactions. The latter are induced by the spin-orbit coupling (SOC), arising from a mismatch between clock wavelength and lattice spacing (17, 18), which lifts the indistinguishability between

spin-polarized fermions on neighboring lattice layers. Systematic exploration of this 1D spin model identified a confinement depth at which the combination of s - and p -wave interactions suppressed detrimental mean-field density shifts (1, 19). Introducing a three-dimensional (3D) lattice confinement for scaling up the density (20) allows further increase of strength of the elastic and inelastic collisions to the point of strongly suppressing all p -wave interactions and making s -wave interactions spectroscopically resolvable (21). Optimizing the atomic coherence times for best clock performance requires balancing lattice-induced Raman scattering and motional dephasing at deep and shallow lattice depths, respectively (22). This study explores different lattice confinement regimes to characterize the impact of higher-order interaction effects, arising from virtual tunneling, on the atomic coherence.

3D lattice spin model

In a 3D lattice filled with a degenerate Fermi gas of spin-polarized ^{87}Sr atoms in the motional ground state (23), the system can be modeled with the Fermi-Hubbard Hamiltonian in which ground and excited state atoms on the same lattice site interact through the Hubbard interaction parameter U , and motion is captured by a tunneling parameter t . In the unity filled limit, a Mott-insulating regime emerges at $U \gg t$, atomic motion is restricted, and atoms interact only through virtual second-order tunneling processes that induce spin-exchange couplings between nearest-neighbor atomic spins known as superexchange (24–26). The physics of superexchange is central in describing magnetic phenomena such as antiferromagnetism (27, 28) and is believed to play a role in superconductivity (29). Several ultracold atom experiments have used optical lattices to explore low-temperature bosonic ferromagnetic and fermionic antiferromagnetic correlations induced by superexchange (30–37), as well as some nonequilibrium superexchange-driven quantum dynamics in local density probes (38–40). With the goal of achieving optimal and scalable clock performance at a unity filled 3D lattice, understanding and controlling the effects of superexchange on collective spin dynamics become necessary (20, 21). The current work using seconds-long Ramsey spectroscopy on tens of thousands of atoms directly probes the coherent nature of superexchange interaction, thus strengthening our understanding of interaction regimes that are favorable for robust quantum coherence and entanglement.

Here we load a degenerate Fermi gas of ^{87}Sr atoms into a 3D lattice with tunable confinement to explore the 3D lattice spin model. The interaction effects on spin coherence between the ground and metastable clock state are directly recorded on Ramsey fringes, which are modulated by coherent superexchange interactions. These experimental observations are well captured by an anisotropic lattice spin model (XXZ plus antisymmetric exchange terms), which breaks the Heisenberg $\text{SU}(2)$ symmetry of the Fermi-Hubbard physics because of the SOC induced by the clock laser (17, 18, 41, 42). Such interactions can also be directly used for the generation of large-scale quantum entanglement over the entire 3D lattice system (43–45).

The experimental schematic is depicted in Fig. 1A. After evaporation, we confine the atoms in a retroreflected, cubic lattice operating at the magic wavelength of $\lambda_{\text{magic}} = 813$ nm with lattice constant $a \approx 407$ nm (20). Beginning with a nuclear spin-polarized Fermi gas with a reduced temperature $T/T_F \approx 0.2$, where T_F is the Fermi temperature, the atoms are adiabatically loaded into the ground band of the 3D lattice (20, 23). In the deep lattice, the initial state is nearly a band insulator with a peak filling of one atom per lattice site (4, 46). The lattice depth (V_{\perp}) of the transverse (horizontal with respect to gravity) confinement is tuned independently from the depth of the vertical confinement (V_z) by adjusting the optical power in the corresponding lattice beams. Our two-level spin system is established between the ground 1S_0 ($|g\rangle$) and metastable electronic “clock” state 3P_0 ($|e\rangle$). We coherently drive the clock transition $|g, m_F = -9/2\rangle \leftrightarrow |e, m_F = -9/2\rangle$

¹JILA, National Institute of Standards and Technology and University of Colorado, Boulder, CO, USA. ²Center for Theory of Quantum Matter, University of Colorado, Boulder, CO, USA.

*Corresponding author. Email: william.milner@colorado.edu (W.R.M.); ye@jila.colorado.edu (J.Y.)

at $\lambda_{\text{clk}} \approx 698$ nm with a vertical laser beam using an optical local oscillator locked to an ultrastable silicon cavity (47).

Ramsey spectroscopy

After loading the lattice, we put the atoms into a superposition of $|g\rangle$ and $|e\rangle$ and perform Ramsey spectroscopy. For detection, in situ absorption imaging along the vertical direction is used and ~ 100 photons per atom are scattered over a 1- μs pulse duration with minimal blurring compared to the diffraction-limited point-spread function of 1.3 μm (4, 46). Two images of the ground and clock state atoms, their numbers denoted N_g and N_e , are taken to determine the excitation fraction $p_e = N_e / (N_e + N_g)$. For a chosen region of interest P_A of our imaged density distribution, we record the local excitation fraction $p_e^A = N_e^A / (N_e^A + N_g^A)$. This is shown in Fig. 1A, where the excitation fractions are evaluated in spatially separate regions P_1 and P_2 to determine both the Ramsey fringe contrast C and relative atomic coherence using imaging spectroscopy (48).

To evaluate atomic coherence that is related to clock performance at different lattice confinement, we measure the Ramsey fringe contrast for varying dark time T . An XY8 sequence consisting of eight π pulses along the two orthogonal rotation axes in the equatorial plane of the Bloch sphere is used to remove single-particle dephasing as depicted in Fig. 2A (49, 50). To decouple the atomic coherence measurement from the finite atom-light coherence time (~ 3 s) (47), the phase of the final Ramsey $\pi/2$ pulse is randomized. Parametric plots of the excitation fractions from concentric regions P_1 and P_2 ($P_1 < 6$ μm and 6 $\mu\text{m} < P_2 < 12$ μm with respect to the trap center) are used to determine the contrast as shown in Fig. 2B. These parametric plots show ellipses, where a maximum likelihood estimator determines the ellipse contrast and jackknifing is used to extract 1σ (standard

deviation) error bars for all Ramsey contrast measurements (48). The system is sufficiently homogeneous in the spatial regions P_1 and P_2 that the contrast is approximately the same (51). No statistically significant phase shift between P_1 and P_2 is measured, indicating that the XY8 pulse sequence largely removes any spatially varying frequency shift.

As a function of dark time T , a stretched exponential function $C_0 e^{-(T/T_2)^\alpha}$ is fit to the Ramsey contrast to extract a T_2 coherence time for $T > 1$ s in order to reject fast transient oscillatory dynamics. For $V_\perp = 0$, we expect different timescales between inter- and intrasite interactions, leading to Gaussian decoherence. We extract a single value $\alpha = 1.38$ by minimizing the combined χ^2 for all measurements for $V_\perp = 0$. For all other measurements with $V_\perp > 0$, we set $\alpha = 1$ when fitting T_2 . The extracted quality factor $Q = \pi C_0 T_2 \nu$ is plotted in Fig. 2C, where ν is the clock transition frequency ≈ 429 THz. We identify three principal regimes: (i) In the 1D lattice regime with no transverse confinement, the longest coherence times are observed; here, the growth of spin excitations caused by on-site and nearest-neighbor interactions is minimized (1, 15, 19). However, inelastic on-site p -wave collisions between excited state atoms during the Ramsey dark time lead to a strong loss in atom number with a $1/e$ lifetime of < 5 s at the density used in this experiment [see fig. S6 in (51)]. In contrast, the atom lifetime in a strong transverse lattice is about 19 s. This renders the 1D limit less favorable for clock operation at high density. (ii) With deep transverse confinement, where the average superexchange coupling strength $\bar{J}_{\text{SE}}/h \gtrsim 1$ Hz, coherent superexchange dynamics are observed on the Ramsey fringe contrast over a timescale of seconds (Figs. 3 and 4). Here, the system consists of individual tubes, and each atom acts as a spin- $1/2$ particle that interacts with its vertical neighbors. As previously reported (22), the deep 3D lattice regime (iii), where $\bar{J}_{\text{SE}}/h \ll 1$ Hz, reveals a limit on the coherence time primarily due to Raman scattering of lattice photons on e atoms. This motivates us to investigate the spin dynamics in the intermediate 3D confinement regime (ii) as potential operating conditions for future 3D lattice clocks. The dark times in this study ($T < 16$ s) are short compared to both the 1S_0 lifetime and vacuum lifetime (51).

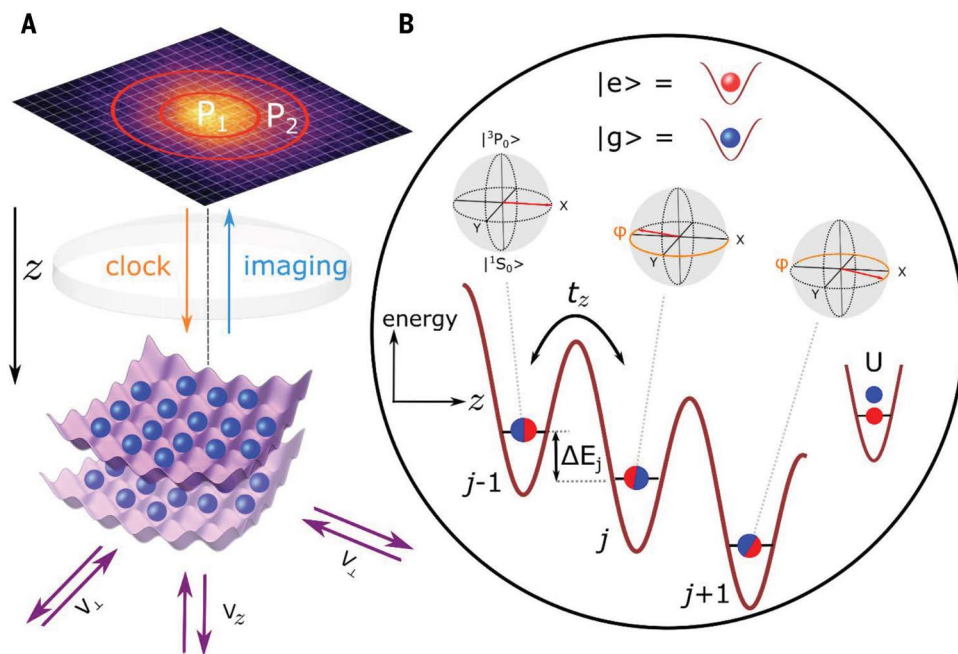


Fig. 1. Experimental setup and interaction model. (A) Ultracold fermions are confined in the ground band of a 3D optical lattice with tunable confinement. Lattice depths can be independently varied by changing the optical power of retro-reflected beams in the transverse direction V_\perp or vertical direction V_z . In situ imaging allows spatially resolved interactions and dephasing by imaging spectroscopy (48). (B) Dynamics are described by the Fermi-Hubbard model with tunneling t_z , interaction energy U , and a site-to-site energy shift ΔE_j from the lattice Gaussian confinement. Atoms along the z axis on sites indexed $j - 1, j$ are initialized in a superposition state of the ground state $|g\rangle = |^1S_0\rangle$ and the metastable electronic state ("clock" state) $|e\rangle = |^3P_0\rangle$, with spin-orbit coupling arising from the phase advancement ϕ of the clock laser between lattice sites. Dephasing of the coherence is proportional to an effective superexchange rate: $4t_z^2 U / (U^2 - \Delta E_j^2)$.

During the Ramsey interrogation time, the atoms interact via the Fermi-Hubbard model presented in Fig. 1B (52). For our fermionic atoms, Fermi statistics forbids two spin-aligned atoms from populating the same lattice site within the ground band. Thus, in the dense limit with one atom per site, only atoms in opposite electronic states can tunnel along the vertical direction z with rate t_z/h and interact with on-site interaction $U = \frac{4\pi\hbar^2}{m} a_{eg-} \int |\mathbf{W}(\mathbf{r})|^4 d^3\mathbf{r}$. These interactions are determined by the s -wave scattering length $a_{eg-} = 69.1(0.9)a_B$ between antisymmetric electronic states (16, 21), and the 3D, single-particle Wannier function $W(\mathbf{r})$ is determined by the lattice confinement. Along the vertical direction, the atoms also experience both the linear gravitational potential and the confinement from the Gaussian transverse lattice beams, leading to an energy offset ΔE_j between adjacent vertical lattice planes indexed by j (53). The clock laser is also launched along the

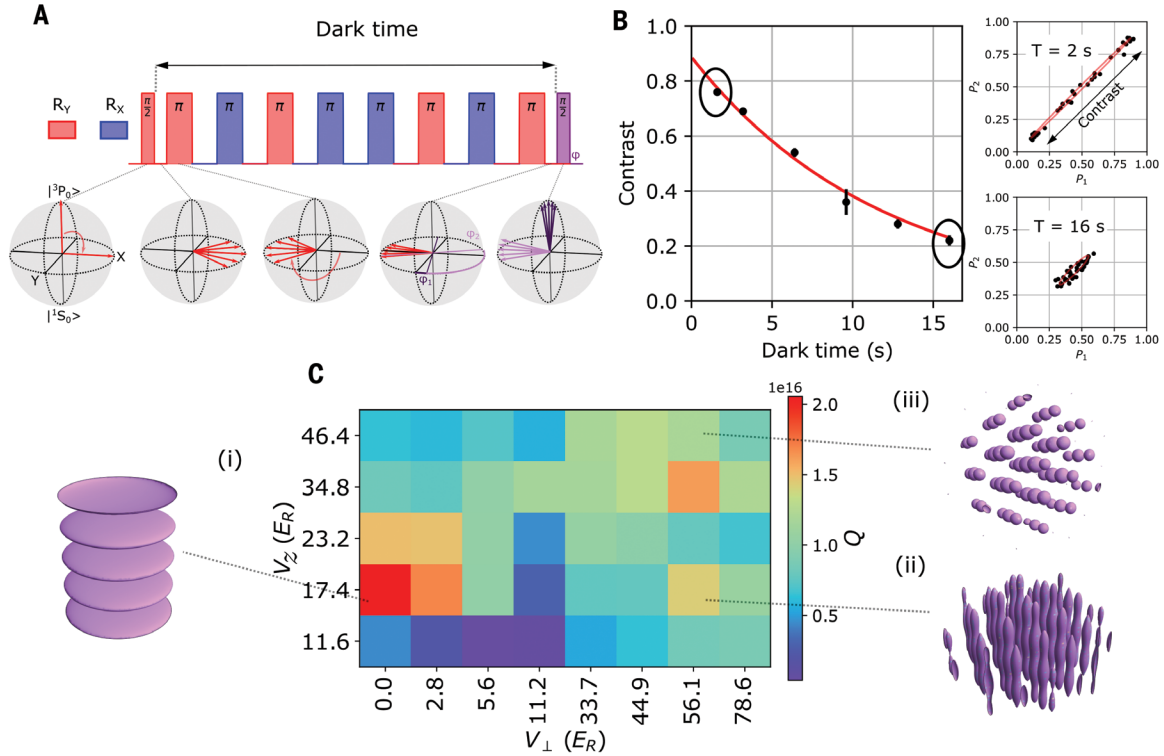


Fig. 2. Coherence time measurement. (A) Ramsey spectroscopy is used to study the coherence time. An XY8 pulse sequence is used to mitigate single-particle dephasing. The dephasing and rephasing of individual spins are depicted on the Bloch sphere during the echo sequence. For the final $\pi/2$ pulse, two choices of the randomized phase $\varphi_{1,2}$ are shown (light and dark purple) to illustrate the spread of resulting excitation fractions in individual realizations. (B) To determine the coherence time T_2 , the contrast decay is fit to a stretched exponential $C(T) = C_0 e^{-(T/T_2)^\nu}$ as a function of dark time T . Insets: The contrast is determined by parametric plots of excitation fractions in regions P_1 and P_2 of the ensemble as depicted in Fig. 1. Error bars are 1σ (standard deviation) obtained from jackknifing. (C) The quality factor $Q = \pi C_0 T_2 \nu$, where $\nu \approx 429$ THz, is plotted over a wide range of transverse and vertical confinement, where $E_R = \hbar^2 / 8ma^2 \approx \hbar \times 3.5$ kHz is the lattice photon recoil energy. Two candidate regimes are identified to investigate further: the weak or zero transverse confinement regime (i), where the longest optical lattice clock T_2 times have been reported (1); and regime (ii), where fast initial contrast decay is observed owing to superexchange interactions. The deep 3D lattice regime (iii) was studied on this platform in (22), where the coherence time is limited by Raman scattering of lattice photons.

vertical direction, setting a spin rotation axis that advances by a phase of $\varphi = 2\pi a / \lambda_{\text{clk}} \approx 7\pi/6$ between neighboring vertical lattice planes, thus inducing SOC (17, 22) as depicted in Fig. 1B. This SOC phase is crucial in facilitating the generation of distinguishable spin states that enable tunneling and with it a path for on-site interaction U and superexchange.

Superexchange interactions

The superexchange oscillations, observed in the 3D confinement regime of our experiment with $V_z < V_{\perp}$ [regime (ii) in Fig. 2C], can be understood from a simple double-well model describing two atoms (spin $s = 1/2$) on two adjacent lattice sites $j = 0, 1$ along the z lattice direction. The Ramsey spectroscopy protocol initializes the atoms in a superposition state $|\Psi_{\text{init}}\rangle = (|g_0\rangle + |e_0\rangle) / \sqrt{2} \otimes (e^{-i\varphi/2}|g_1\rangle + e^{i\varphi/2}|e_1\rangle) / \sqrt{2}$. Crucially, owing to the differential laser phase φ , aside from a global phase this initial state is an admixture of the spin triplet and singlet states, with $|\Psi_{\text{init}}\rangle \sim e^{-i\varphi/2}|g, g\rangle + e^{i\varphi/2}|e, e\rangle + \cos(\varphi/2)(|g, e\rangle + |e, g\rangle) + i\sin(\varphi/2)(|g, e\rangle - |e, g\rangle)$. At half-filling and in the strongly interacting limit $U \gg t_z$, superexchange interactions arising between neighboring spins, $J_{\text{SE}} \hat{\mathbf{s}}_0 \cdot \hat{\mathbf{s}}_1$, introduce an energy shift for the singlet state, which translates to a phase difference $J_{\text{SE}} T$ compared to the triplet states during the coherent evolution time T . Here $\hat{\mathbf{s}}_j = (\hat{s}_j^X, \hat{s}_j^Y, \hat{s}_j^Z)$, with \hat{s}_j^l referring to spin-1/2 matrices describing atoms on sites j in the lab frame.

More formally, we rotate into a “spiral” frame where the initial state is uniform (all atoms in the same superposition state) and the site-dependent laser phase φ is absorbed into the spin operators across

the lattice, $\hat{s}_j^{\pm} = \hat{s}_j^{\pm} e^{\pm i\varphi}$, $\hat{s}_j^Z = \hat{s}_j^Z$. Thus, we obtain a superexchange spin Hamiltonian in the spiral frame

$$\hat{H}_{\text{SE}} = \sum_j J_{\text{SE}}(j) \left[\frac{1}{2} \left(e^{i\varphi} \hat{s}_j^+ \hat{s}_{j+1}^- + H.c. \right) + \hat{s}_j^Z \hat{s}_{j+1}^Z \right] \quad (1)$$

The superexchange interaction strength is $J_{\text{SE}}(j) = 4t_z^2 U / (U^2 - \Delta E_j^2)$, which is inhomogeneous owing to the local potential difference between adjacent sites ΔE_j , including gravity and the lattice Gaussian confinement. Furthermore, the spiral phase makes this spin Hamiltonian go beyond conventional superexchange interactions in optical lattices, as it exhibits exchange-symmetric XXZ-style anisotropy and an anti-symmetric spin exchange term (51). Observables such as atomic coherence reveal collective quantum dynamics on timescales of the averaged \bar{J}_{SE} over the ensemble, which is tuned by controlling the inhomogeneity and the lattice depth.

In Fig. 3, A and B, we show the contrast decay as a function of dark time for $V_{\perp} > V_z$, finding a clear oscillatory feature on timescales of the superexchange rate \bar{J}_{SE} . For these measurements, V_z is fixed to $17.4 E_R$ at which $t_z \approx \hbar \times 14.2$ Hz, where $E_R = \hbar^2 / 8ma^2 \approx \hbar \times 3.5$ kHz is the lattice photon recoil energy. \bar{J}_{SE} is tuned by varying V_{\perp} between 19.7 and $67.4 E_R$, thus varying U / \hbar from 1.2 to 2.3 kHz. In the $V_{\perp} \gg V_z$ regime, the system is composed of isolated vertical tubes along z as shown in Fig. 2C. We assume that all atoms within each tube are pinned in place even for non-unity filling, because the local potential difference is much stronger than tunneling ($\Delta E_j \gg t_z$). We further

assume that every uninterrupted chain of neighboring atoms within a given tube undergoes evolution under the superexchange Hamiltonian \hat{H}_{SE} . Their evolution is independent of other chains, and the contrast is an average over all chains. The curves in Fig. 3, A and B, show numerical predictions averaging over the full 3D system using calibrated experimental parameters and an optimized temperature, and include the overall slow decay in contrast reported in Fig. 2C, which find good agreement with the measurements. The extracted temperatures in the lattice indicate that our experiments operate at a central filling fraction of ≈ 0.5 ground-band atoms per lattice site.

To extract the superexchange rates, we vary V_{\perp} and fit the experimentally measured contrast decay to the function $C_{SE}(T) = Ae^{-T/T_2} + B\cos(2\pi fT)e^{-T/T_{osc}} + D$. In Fig. 3C, the measured oscillation frequencies f are first compared to results derived from the same full many-body Hamiltonian used to generate the theory curves in Fig. 3, A and B (empty red squares). Here, the oscillation frequencies are extracted in the same way as for the measurement data. Additionally, we are

also using a simplified theoretical model that averages over contributions of two-site pairs (blue line), which is expected to be valid for low-to-intermediate filling fractions, where long chains are unlikely. This calculation includes higher-order interaction effects such as bond-charge corrections to the tunneling rate t_2 (5I). The agreement with both theoretical models is excellent for intermediate V_{\perp} between 22.5 and $45 E_R$. For the deepest V_{\perp} , the experimentally measured rate appears to be higher frequency. Numerical calculations suggest this could arise from additional interaction inhomogeneity or light-scattering effects (54) that favor higher-frequency contributions. At shallow $V_{\perp} < 20E_R$, where $V_{\perp} \approx V_{zp}$, our theoretical approximation of isolated vertical tubes breaks down and in-plane interactions become relevant. In Fig. 3D, the dark times of the contrast decay data are rescaled by the calculated superexchange rate from the two-site model (blue line in Fig. 3C). The rescaled data collapse to a single curve, reflecting the underlying superexchange dynamics in all measurements. This is also in agreement with a more general theoretical model that attempts to

capture the effects of finite temperature and trap inhomogeneity without explicitly invoking experimental details. Instead, the superexchange couplings and chain lengths are randomly sampled from probability distributions that aim to capture the experimental parameters and inhomogeneity (5I). We do not expect perfect rescaling owing to varying $J_{SE}(j)$ inhomogeneity caused by a change in lattice curvature as a function of V_{\perp} .

Controlling superexchange interactions

To study the properties of the interactions further, we vary the lattice filling and the energy offsets ΔE_j of the local lattice tilt in Fig. 4. First, the fraction of atoms participating in superexchange is reduced by imprinting holes in the lattice. Beginning with maximum filling, before Ramsey spectroscopy, a variable clock laser pulse area is used to shelve atoms in e with spatially uniform probability, and subsequently the remaining g atoms are removed with resonant light at 461 nm (Fig. 4A). The ensuing contrast decay as a function of the total atom number N is plotted in Fig. 4B. The oscillation amplitude, reflecting the fraction of atoms participating in superexchange, is strongly decreased as N is reduced owing to the increasing number of holes. Because of the reduced filling fraction at the wings of the atom cloud, this effect is also observed when choosing the region of interest to be an annulus and increasing its radius compared to P_2 [fig. S4 in (5I)].

As the position of the atoms in the combined potential of gravity and the lattice confinement is shifted vertically, the site-to-site energy shift ΔE_j , and consequently the superexchange interaction strength, is strongly modified. We precisely move the cloud position at the micrometer scale (5I). Figure 4D displays the resulting oscillations for several values

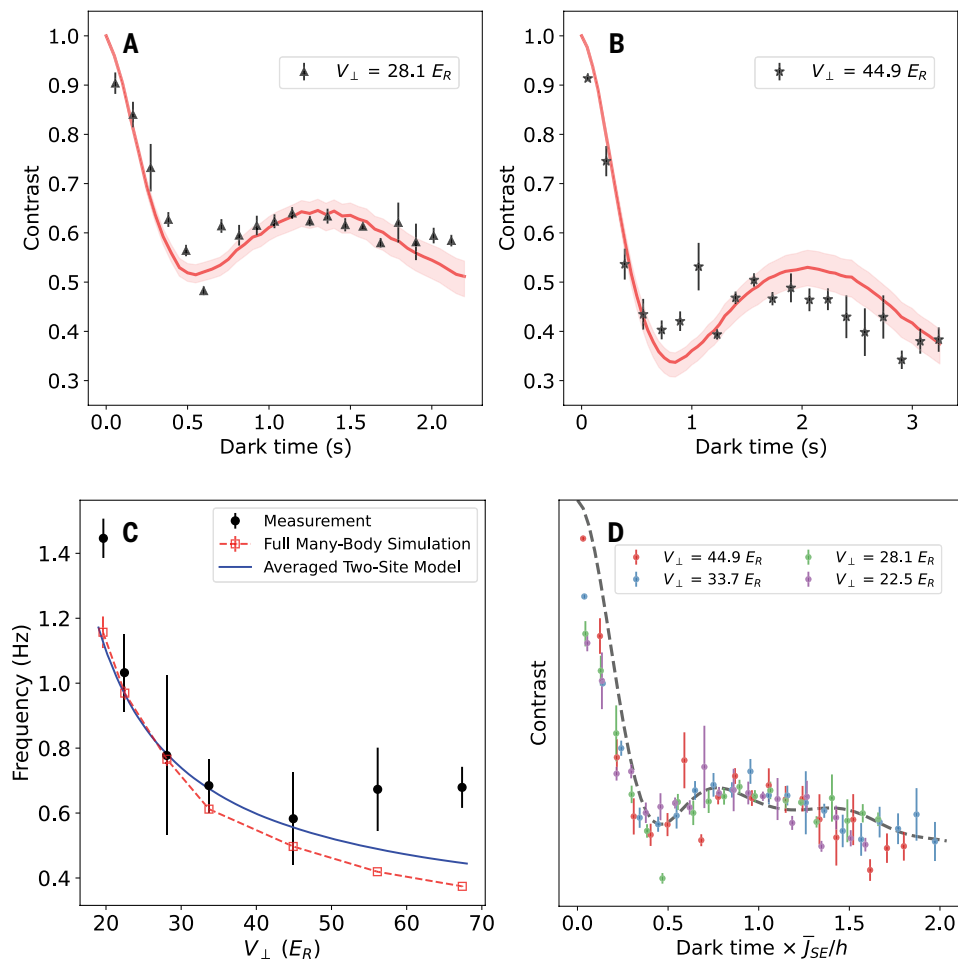


Fig. 3. Observing superexchange interactions. Ramsey contrast decay is studied in a 3D lattice at fixed $V_z = 17.4 E_R$ and thus t_z , while V_{\perp} is varied between ~ 70 and $20 E_R$ primarily modifying U . Decay curves at (A) $V_{\perp} = 28.1 E_R$ and (B) $44.9 E_R$ are plotted. Error bars are 1σ (standard deviation). Red lines are calculated averaging contrast decay in 1D chains initialized from a thermal distribution of the 3D cloud with fitted temperatures of $350(14)$ nK for $V_{\perp} = 28.1 E_R$ and $322(17)$ nK for $V_{\perp} = 44.9 E_R$ (5I). The error bands stem from the uncertainty on the temperature and T_2 . (C) Fitted contrast oscillation frequencies (black points) are compared to the fit results obtained from the full simulations as shown in (A) and (B) (red empty squares) and calculated superexchange frequency (blue line) including bond-charge corrections to t_2 , which averages the expected oscillations with local ΔE_j and U along the imaging direction. Error bars are 1σ (standard deviation) uncertainty of the fitted frequency. (D) Contrast curves approximately collapse when dark times are rescaled by the calculated oscillation frequency (blue line in Fig. 3C). A simple simulation sampling spin chains with different lengths and coupling strengths (gray dashed line) is overlaid.

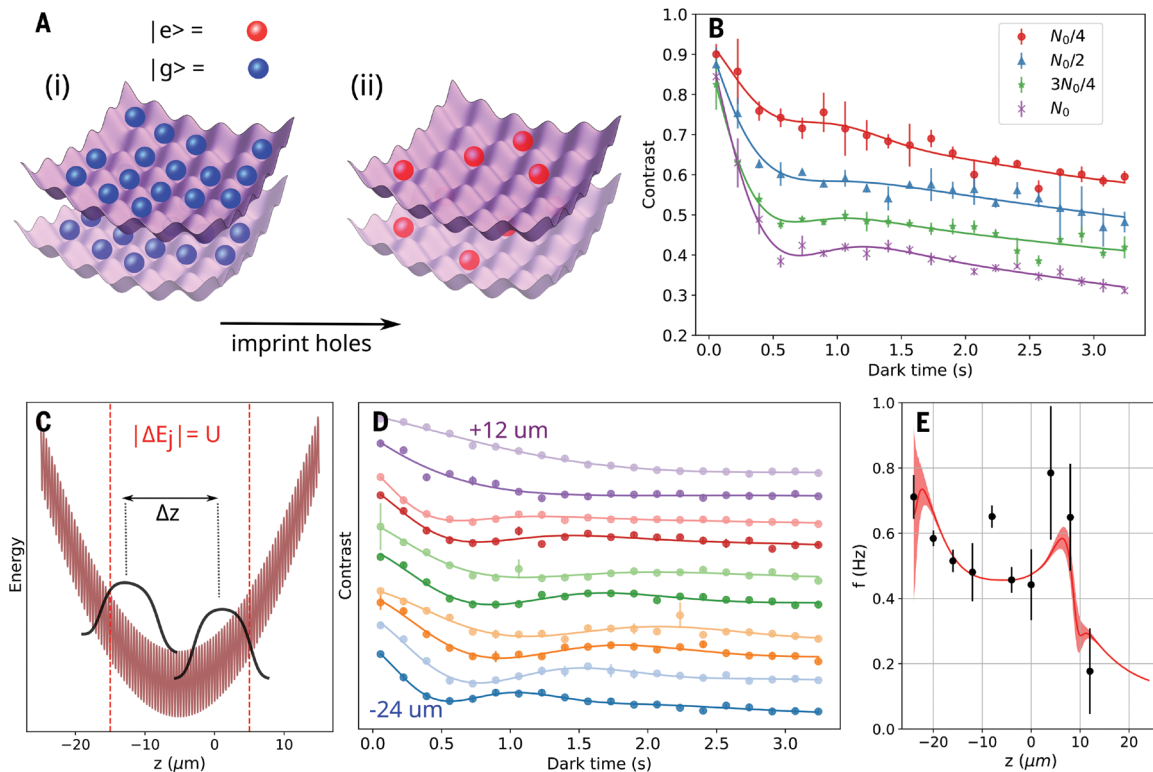


Fig. 4. Controlling superexchange interactions. All measurements presented here are performed at trap depths $V_z = 17.4 E_R$ and $V_\perp = 44.9 E_R$. **(A)** The fraction of atoms participating in superexchange is modified by reducing the filling fraction by uniformly adding holes. In (i), the initial state is a highly filled sample of ground state atoms. Next, atoms are placed in a superposition state with tunable pulse area. Light resonant with $|^1S_0\rangle$ is turned on to imprint holes, with the remaining atoms in $|^3P_0\rangle$ as shown in (ii). **(B)** The contrast decay as the clock pulse area and thus total atom number N is reduced compared to the initial atom number N_0 . The solid lines shown in (B) and (D) are fits using the model $C_{SE}(T)$ provided in the main text. Error bars are 1σ (standard deviation). **(C)** The superexchange coupling is modified by changing the position of the atoms in the lattice potential, which varies the site-to-site energy shift ΔE_j . Representative density distributions for the cloud at different positions are given by black solid lines. At the positions indicated by vertical red lines, tunneling becomes resonant and strongly enhances the local $J_{SE}(j)$. However, averaged over the whole cloud, this only slightly modifies the oscillation frequencies. **(D)** Oscillations in contrast at different vertical positions z ; curves are shifted vertically according to z position. **(E)** These measured oscillation frequencies are compared with a heuristic superexchange simulation (red line) of the Ramsey contrast (51).

of the cloud position z . We compare the oscillation frequency with the simplified simulation averaging over two-site pairs in Fig. 4E (red line), similar to the blue line shown in Fig. 3C. Averaging the Ramsey signal along the z -direction during imaging strongly suppresses the effect of locally enhanced $J_{SE}(j)$, where $U = \Delta E_j$. The asymmetry of the background trap gradient around $z = 0$ leads to a reduction in the oscillation frequency at large z where $\Delta E_j > U$. The frequency of the simulation shows qualitative agreement with the measured oscillation.

Discussion and outlook

Superexchange interactions are identified as an important systematic effect that degrades the precision of optical lattice clocks operating with high filling at timescales h/\bar{J}_{SE} . For clock metrology, we can either reduce the magnitude or control the form of the superexchange interactions to enhance clock performance. For example, we can increase the lattice constant a sufficiently to reduce the tunneling rate to a negligible value (22). Alternatively, a variable lattice spacing can be used to make a commensurate with λ_{clk} to achieve $\varphi \bmod 2\pi = 0$. Without SOC ($\varphi \bmod 2\pi = 0$), the isotropic Heisenberg Hamiltonian $\sum_j J_{SE}(j) \hat{\mathbf{s}}_j \cdot \hat{\mathbf{s}}_{j+1}$ is recovered, and any coherent spin state becomes an eigenstate accumulating only a trivial global phase.

Collective superexchange interactions can also be used to produce spin entanglement for quantum enhanced sensing (45). A promising

parameter regime for implementing this strategy is around region (i) identified in Fig. 2C. Although in the 1D limit with $V_\perp = 0$ we obtain the maximal value of the coherence time T_2 , the amount of usable entanglement in this regime is limited (15) owing to the presence of strong p -wave loss. However, we observe that the transition from pancakes to “waffles” by introducing a weak transverse corrugation of $V_\perp \gtrsim 5E_R$ strongly reduces the atom loss by increasingly localizing the atoms in the transverse directions (51). Thanks to the lack of clock-induced SOC within each waffle, the in-plane superexchange leads to isotropic Heisenberg interactions, which feature energy gaps between sectors with different total spin length. Thus, by reducing single-particle inhomogeneities via potential shaping or layer selection (55), the superexchange interactions investigated in this work can not only energetically lock the atoms in collective spins across all horizontal planes but also subsequently couple and entangle them through the SOC-induced XXZ interaction along the vertical direction.

REFERENCES AND NOTES

1. T. Bothwell *et al.*, *Nature* **602**, 420–424 (2022).
2. A. Aepli, K. Kim, W. Warfield, M. S. Safronova, J. Ye, *Phys. Rev. Lett.* **133**, 023401 (2024).
3. S. Kolkowitz *et al.*, *Phys. Rev. D* **94**, 124043 (2016).
4. R. B. Hutson, W. R. Milner, L. Yan, J. Ye, C. Sanner, *Science* **383**, 384–387 (2024).
5. Boulder Atomic Clock Optical Network (BACON) Collaboration, *Nature* **591**, 564–569 (2021).

6. N. Nemitz *et al.*, *Nat. Photonics* **10**, 258–261 (2016).
7. W. F. McGrew *et al.*, *Nature* **564**, 87–90 (2018).
8. W. M. Itano *et al.*, *Phys. Rev. A* **47**, 3554–3570 (1993).
9. E. Pedrozo-Peñafiel *et al.*, *Nature* **588**, 414–418 (2020).
10. J. M. Robinson *et al.*, *Nat. Phys.* **20**, 208–213 (2024).
11. W. J. Eckner *et al.*, *Nature* **621**, 734–739 (2023).
12. J. Franke *et al.*, *Nature* **621**, 740–745 (2023).
13. E. Oelker *et al.*, *Nat. Photonics* **13**, 714–719 (2019).
14. A. D. Ludlow, M. M. Boyd, J. Ye, E. Peik, P. O. Schmidt, *Rev. Mod. Phys.* **87**, 637–701 (2015).
15. M. J. Martin *et al.*, *Science* **341**, 632–636 (2013).
16. X. Zhang *et al.*, *Science* **345**, 1467–1473 (2014).
17. S. Kolkowitz *et al.*, *Nature* **542**, 66–70 (2017).
18. S. L. Bromley *et al.*, *Nat. Phys.* **14**, 399–404 (2018).
19. A. Aeppli *et al.*, *Sci. Adv.* **8**, eadc9242 (2022).
20. S. L. Campbell *et al.*, *Science* **358**, 90–94 (2017).
21. A. Goban *et al.*, *Nature* **563**, 369–373 (2018).
22. R. B. Hutson *et al.*, *Phys. Rev. Lett.* **123**, 123401 (2019).
23. L. Sonderhouse *et al.*, *Nat. Phys.* **16**, 1216–1221 (2020).
24. L.-M. Duan, E. Demler, M. D. Lukin, *Phys. Rev. Lett.* **91**, 090402 (2003).
25. M. Lewenstein *et al.*, *Adv. Phys.* **56**, 243–379 (2007).
26. S. Trotzky *et al.*, *Science* **319**, 295–299 (2008).
27. E. Manousakis, *Rev. Mod. Phys.* **63**, 1–62 (1991).
28. A. Auerbach, *Interacting Electrons and Quantum Magnetism* (Springer, 2012); <https://link.springer.com/book/10.1007/978-1-4612-0869-3>.
29. P. A. Lee, N. Nagaosa, X.-G. Wen, *Rev. Mod. Phys.* **78**, 17–85 (2006).
30. D. Greif, T. Uehlinger, G. Jotzu, L. Tarruell, T. Esslinger, *Science* **340**, 1307–1310 (2013).
31. R. A. Hart *et al.*, *Nature* **519**, 211–214 (2015).
32. M. Boll *et al.*, *Science* **353**, 1257–1260 (2016).
33. L. W. Cheuk *et al.*, *Science* **353**, 1260–1264 (2016).
34. A. Mazurenko *et al.*, *Nature* **545**, 462–466 (2017).
35. M. Takahashi, *Thermodynamics of One-Dimensional Solvable Models* (Cambridge Univ. Press, 2005); <https://www.cambridge.org/core/books/thermodynamics-of-one-dimensional-solvable-models/B74C2EB63A89A1E5D7347EE48E4AFD6C>.
36. S. Taie *et al.*, *Nat. Phys.* **18**, 1356–1361 (2022).
37. M. Gall, N. Wurz, J. Samland, C. F. Chan, M. Köhl, *Nature* **589**, 40–43 (2021).
38. R. C. Brown *et al.*, *Science* **348**, 540–544 (2015).
39. P. N. Jepsen *et al.*, *Nature* **588**, 403–407 (2020).
40. H. Sun *et al.*, *Nat. Phys.* **17**, 990–994 (2021).
41. M. Mamaev, I. Kimchi, R. M. Nandkishore, A. M. Rey, *Phys. Rev. Res.* **3**, 013178 (2021).
42. P. N. Jepsen *et al.*, *Nat. Phys.* **18**, 899–904 (2022).
43. P. He *et al.*, *Phys. Rev. Res.* **1**, 033075 (2019).
44. T. Hernández Yanes *et al.*, *Phys. Rev. Lett.* **129**, 090403 (2022).
45. M. Mamaev, D. Barberena, A. M. Rey, *Phys. Rev. A* **109**, 023326 (2024).
46. W. R. Milner, L. Yan, R. B. Hutson, C. Sanner, J. Ye, *Phys. Rev. A* **107**, 063313 (2023).
47. D. G. Matei *et al.*, *Phys. Rev. Lett.* **118**, 263202 (2017).
48. G. E. Marti *et al.*, *Phys. Rev. Lett.* **120**, 103201 (2018).
49. T. Gullion, D. B. Baker, M. S. Conradi, *J. Magn. Reson.* **89**, 479–484 (1990).
50. J.-R. Li *et al.*, *Nature* **614**, 70–74 (2023).
51. See supplementary materials.
52. T. Esslinger, *Annu. Rev. Condens. Matter Phys.* **1**, 129–152 (2010).
53. P. Lemonde, P. Wolf, *Phys. Rev. A* **72**, 033409 (2005).
54. M. Foss-Feig, K. R. A. Hazzard, J. J. Bollinger, A. M. Rey, *Phys. Rev. A* **87**, 042101 (2013).
55. A. L. Gaunt, T. F. Schmidutz, I. Gotlibovych, R. P. Smith, Z. Hadzibabic, *Phys. Rev. Lett.* **110**, 200406 (2013).
56. W. R. Milner *et al.*, Coherent evolution of superexchange interaction in seconds long optical clock spectroscopy, Data and code, Dryad (2024); <https://doi.org/10.5061/dryad.qv9s4mwq5>.

ACKNOWLEDGMENTS

We thank A. Aeppli, Z. Hu, J. Hur, D. Kedar, K. Kim, M. Miklos, J. M. Robinson, Y. M. Tso, W. Warfield, and Z. Yao for useful discussions. We thank A. M. Kaufman and N. D. Opong for careful reading of the manuscript and for providing insightful comments. **Funding:** Funding for this work is provided primarily by the DOE Center of Quantum System Accelerator and by NSF QLCI OMA-2016244, NSF JILA-PFC PHY-2317149, Va. Bush Fellowship, AFOSR FA9550-24-1-0179, and NIST. B.L. acknowledges funding from the Lindemann Trust and S.L. from the Alexander von Humboldt Foundation. **Author contributions:** The experiment was performed by W.R.M., S.L., L.Y., B.L., M.N.F., R.B.H., and J.Y. The theory model was developed by M.M., A.C., and A.M.R. All authors contributed to data analysis and writing of the manuscript. **Competing interests:** The authors declare no competing interests. **Data and materials availability:** Experimental data and analysis code are archived at Dryad (56). **License information:** Copyright © 2025 the authors, some rights reserved; exclusive licensee American Association for the Advancement of Science. No claim to original US government works. <https://www.sciencemag.org/about/science-licenses-journal-article-reuse>

SUPPLEMENTARY MATERIALS

science.org/doi/10.1126/science.ado5987
 Materials and Methods; Supplementary Text; Figs. S1 to S6; Table S1; References (57, 58)
 Submitted 9 February 2024; resubmitted 17 July 2024; accepted 13 March 2025

10.1126/science.ado5987